



# Novel $\alpha$ -Fe<sub>2</sub>O<sub>3</sub>/TiO<sub>2</sub> nanocomposites with enhanced photocatalytic activity

Houda Mansour<sup>1</sup> · K. Omri<sup>2,3</sup> · Radhouane Bargougui<sup>1</sup> · Salah Ammar<sup>1</sup>

Received: 11 September 2019 / Accepted: 18 January 2020 / Published online: 3 February 2020  
© Springer-Verlag GmbH Germany, part of Springer Nature 2020

## Abstract

In this study, hematite–anatase ( $\alpha$ -Fe<sub>2</sub>O<sub>3</sub>/TiO<sub>2</sub>) nanocomposites were prepared successfully using a simple co-precipitation method. The obtained samples were characterized using X-ray diffraction (XRD), Raman spectroscopy, transmission electron microscopy (TEM), UV–visible diffuse-reflectance spectroscopy (DRS), and a vibrating sample magnetometer (VSM). Experimental results demonstrate that  $\alpha$ -Fe<sub>2</sub>O<sub>3</sub>@TiO<sub>2</sub> nanocomposites are spherical in shape with average sizes close to 38 nm. In addition, the photocatalytic activities of the composites samples were studied based on the degradation of methylene blue (MB) as a model compound, where the results illustrated that the  $\alpha$ -Fe<sub>2</sub>O<sub>3</sub>@50% TiO<sub>2</sub> nanocomposites performed the best as a photocatalyst under visible light. These nanocomposites samples provide a positive example for the fabrication of other structures for photocatalysis or other applications.

**Keywords** Micro-structural · Methylene blue · Photocatalytic activity ·  $\alpha$ -Fe<sub>2</sub>O<sub>3</sub>@TiO<sub>2</sub> nanocomposites

## 1 Introduction

In recent years, considerable studies have been carried out for the elimination of organic pollutants through photocatalytic degradation [1–3]. Among diverse oxide semiconductor photocatalysts, hematite ( $\alpha$ -Fe<sub>2</sub>O<sub>3</sub>) can be used as visible-light photocatalyst, due to its narrow band gap of 2.2 eV, which exhibits excellent properties such as non-toxicity, natural abundance, and strong oxidation power [4, 5]. Furthermore, the magnetic properties of hematite ( $\alpha$ -Fe<sub>2</sub>O<sub>3</sub>) are good in the water treatment, because it can be conveniently separated by magnetic separation technology [6]. Nevertheless, the use of  $\alpha$ -Fe<sub>2</sub>O<sub>3</sub> nanoparticles in photocatalytic process exhibits a rapid recombination of the electron–hole after the photo excitation of  $\alpha$ -Fe<sub>2</sub>O<sub>3</sub>, which leads to a decrease in

the photo-degradation activity [7, 8]. To resolve this limitation, coupling TiO<sub>2</sub> with  $\alpha$ -Fe<sub>2</sub>O<sub>3</sub> forms core–shell nanostructures have been considered as one of the most promising structures for the purpose of preventing recombination of electron–hole pairs [8–10]. As well known, anatase phase of TiO<sub>2</sub> nanoparticles has attracted extensive attention due to their physical and chemical properties such as non-toxicity, high photochemical corrosive resistance, and strong oxidizing power [11, 12].

Up to now, a diversity of techniques have been developed to prepare  $\alpha$ -Fe<sub>2</sub>O<sub>3</sub>@TiO<sub>2</sub> nanocomposites, including sol–gel method [13, 14], hydrothermal technique [9, 15, 16], deposition [17–19], template-assisted method [16, 20], heteroepitaxial growth route [21], and chemical co-precipitation [22, 23]. Unlike the other methods, chemical co-precipitation has proved to be the most applied and most effective route to fabricate nanocomposites samples due to its short preparation time, low cost, high purity, simple preparation, and low operation temperature. Besides, the co-precipitation method is conducted through an aqueous process, enabling satisfactory solubility, homogeneous distribution of doping element, and control of stoichiometry.

Many works reported the synthesis of hematite–anatase ( $\alpha$ -Fe<sub>2</sub>O<sub>3</sub>@TiO<sub>2</sub>) nanocomposites. Suiyuan et al. [24] elaborated the Fe<sub>2</sub>O<sub>3</sub>–TiO<sub>2</sub> nanocomposite particles in a liquid-phase system with 80 wt% ethylene glycol and 20

✉ K. Omri  
omrikarim16@gmail.com

<sup>1</sup> Faculté des Sciences de Gabès, UR Electrochimie, Matériaux et Environnement, Université de Gabès, Cite Erriadh, 6072 Gabès, Tunisia

<sup>2</sup> Laboratory of Physics of Materials and Nanomaterials Applied At Environment (LaPhyMNE), Faculty of Sciences in Gabes, Gabes University, Gabès, Tunisia

<sup>3</sup> College of Science and Arts, Sajir, University of Shaqra, Shaqra, Saudi Arabia

wt% deionized water using pulsed laser gas-phase evaporation–liquid-phase collection. The morphology, structure, magnetic properties, and synthesis mechanism of the samples were studied by means of transmission electron microscopy, X-ray diffraction, infrared spectroscopy, and vibration magnetometer. The results indicate that the Fe<sub>2</sub>O<sub>3</sub>–TiO<sub>2</sub> nanocomposite particles are spherical, and diameters of the primary particles range from 20 to 50 nm. With the increase of Fe<sub>2</sub>O<sub>3</sub> in content, the magnetic saturation intensity and coercivity of Fe<sub>2</sub>O<sub>3</sub>–TiO<sub>2</sub> nanocomposite particles both increase. In another study [13], sol–gel technique was used to synthesize TiO<sub>2</sub>–Fe<sub>2</sub>O<sub>3</sub> nanocomposites with various Fe<sub>2</sub>O<sub>3</sub> weight percentages. The physicochemical properties of the samples were examined by XRD, XRF, SEM, EDX, HRTEM, UV–Vis DRS, FTIR, TGA, and nitrogen gas physisorption studies. The effects of calcination temperatures and Fe<sub>2</sub>O<sub>3</sub> content on the mesostructure and photocatalytic strength of the prepared TiO<sub>2</sub>–Fe<sub>2</sub>O<sub>3</sub> composites were investigated. Results showed that composites with distinct structural, optical, and photochemical properties can be formed by varying Fe<sub>2</sub>O<sub>3</sub> content. Yubing et al. [21] reported the synthesis of  $\alpha$ -Fe<sub>2</sub>O<sub>3</sub>@TiO<sub>2</sub> core–shell via a heteroepitaxial growth route using the  $\alpha$ -Fe<sub>2</sub>O<sub>3</sub> spindle as a hard template display improved photocatalytic degradation activity for Rhodamine B dye under visible-light irradiation. The results indicate that the  $\alpha$ -Fe<sub>2</sub>O<sub>3</sub>@TiO<sub>2</sub> core–shell nanocomposite with an optimal molar ratio of 7% for  $\alpha$ -Fe<sub>2</sub>O<sub>3</sub>:TiO<sub>2</sub> exhibits the best photocatalytic performance under visible-light irradiation. The literature survey shows that quest for finding inexpensive and simple methods for fabricating  $\alpha$ -Fe<sub>2</sub>O<sub>3</sub>@TiO<sub>2</sub> core–shell nanocomposites is continuing [20, 21, 25]. Research for new approaches of synthesizing  $\alpha$ -Fe<sub>2</sub>O<sub>3</sub>@TiO<sub>2</sub> nanocomposites samples with improved physical and chemical characteristics is ongoing.

In this study,  $\alpha$ -Fe<sub>2</sub>O<sub>3</sub>@TiO<sub>2</sub> nanocomposites were synthesized by co-precipitation method. The crystalline structure, morphological, optical, and magnetic properties of elaborated samples were examined using X-ray diffraction (XRD), spectroscopy RAMAN, transmission electron microscopy (TEM), UV–visible diffuse-reflectance spectroscopy (UV/DRS), and a vibrating sample magnetometer (VSM). Subsequently, the photocatalytic activity of  $\alpha$ -Fe<sub>2</sub>O<sub>3</sub>@TiO<sub>2</sub> nanocomposites on the degradation of MB was investigated in detail.

## 2 Experimental

### 2.1 Material synthesis

All chemicals used here were analytical-grade and without further purification. Hematite ( $\alpha$ -Fe<sub>2</sub>O<sub>3</sub>) nanoparticles were prepared via the chemical precipitation route. In a

typical experiment, 0.1 M FeCl<sub>3</sub>, 6H<sub>2</sub>O was dissolved in ultrapure water under vigorous stirring, which was continuously stirred for 1 h at a temperature of 80 °C. Next, aqueous ammonia solution (28%) was added to adjust the pH value to 11 and the solution was kept at this pH for 3 h to fully obtain the hydroxide phase. After cooling at room temperature, red precipitates were obtained which were collected by centrifugation and washed ultrapure water until all of the chloride ions were leached from the filtered material. The wet material was then dried at 80 °C for 12 h and then calcined at 700 °C for 4 h.

$\alpha$ -Fe<sub>2</sub>O<sub>3</sub>@TiO<sub>2</sub> nanocomposite samples with different TiO<sub>2</sub> contents were fabricated via the co-precipitation method: 0.1 M of hematite ( $\alpha$ -Fe<sub>2</sub>O<sub>3</sub>) nanoparticles was introduced to ethanol and sonicated for 30 min. Titanium (IV) isopropoxide (TTIP) (10% and 50%) was added dropwise into the resultant dispersion and the mixture was vigorously stirred on the magnetic stirrer at 80 °C. Precipitation of TiO<sub>2</sub> on the surface of  $\alpha$ -Fe<sub>2</sub>O<sub>3</sub> was performed by slow drop-wise addition of the ammonia aqueous solution (28%). After 3 h, the resulting  $\alpha$ -Fe<sub>2</sub>O<sub>3</sub>@TiO<sub>2</sub> was recovered by centrifugation, rinsed several times, dried for 12 h at 80 °C, and calcined for 3 h at 500 °C. Moreover, the schematic illustration of the preparation of  $\alpha$ -Fe<sub>2</sub>O<sub>3</sub>@TiO<sub>2</sub> nanocomposites is shown in Scheme 1.

To investigate the influence of the TiO<sub>2</sub> shell nanoparticles on the preparation of  $\alpha$ -Fe<sub>2</sub>O<sub>3</sub>@TiO<sub>2</sub> nanocomposites, anatase (TiO<sub>2</sub>) was used for comparison which was synthesized by the co-precipitation method according to our previous report [12].

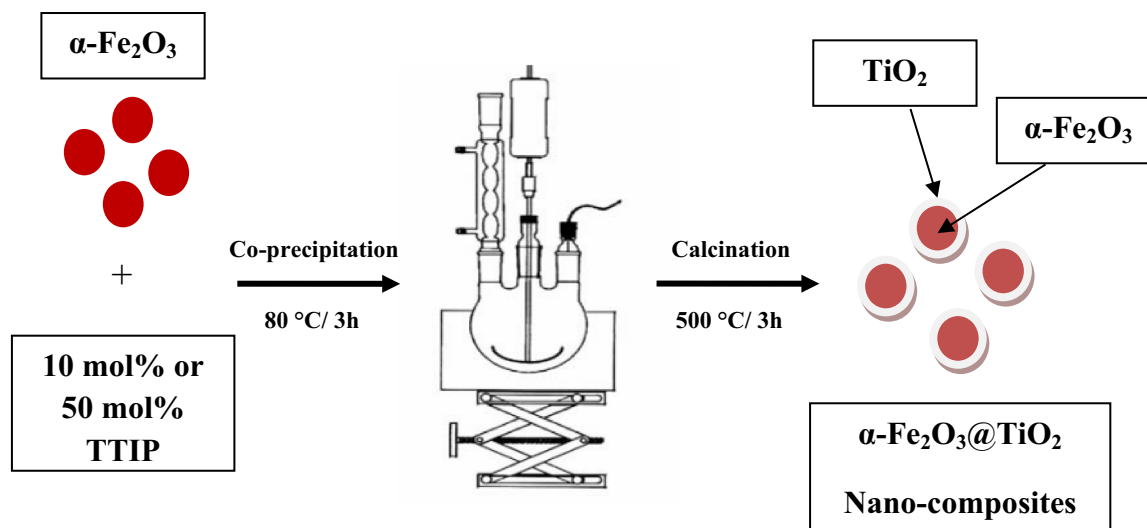
### 2.2 Characterization

XRD measurements were acquired using a D8-Advance Bruker diffractometer with Cu-K $\alpha$  radiation ( $\lambda = 0.15406$  nm) over a  $2\theta$  range of 20°–80° and with an angle step size of 0.02°. The average crystallite size ( $D$ ) of all samples can be estimated from the XRD patterns using Debye–Scherrer formula [26]:

$$D = \frac{K\lambda}{\beta \cos \theta}, \quad (1)$$

where  $D$  is the crystallite size of the hematite ( $\alpha$ -Fe<sub>2</sub>O<sub>3</sub>) nanoparticles (in nm),  $K$  is a constant related to the crystallite shape (0.9),  $\lambda = 0.154056$  nm is the wavelength of Cu-K $\alpha$  radiation,  $\beta$  is the full width at half maximum (FWHM) of the most intense peak (104) (in radians), and  $\theta$  is the diffraction angle (in radians).

Raman spectra were collected using a Renishaw Raman microscope with excitation at 633 nm. The morphology and sizes of the particles in the samples were analyzed by TEM



**Scheme 1** Schematic illustration of the synthetic chemistry and the formation process of  $\alpha$ -Fe<sub>2</sub>O<sub>3</sub>@TiO<sub>2</sub> nanocomposites

(JEOL 2100, FEG-TEM 200 kV) and scanning electron microscope (Hitachi 4160-F, SEM).

UV–Vis/DRS spectra were obtained with a UV–Vis spectrometer (Shimadzu UV-3101 PC) equipped with an integrating sphere, and baseline correction was performed using a calibrated reference sample of powdered barium sulfate (BaSO<sub>4</sub>). The band-gap energy of the samples was determined according to Tauc expression [27]:

$$(\alpha h\nu) = A(h\nu - E_g)^n, \quad (2)$$

where  $\alpha$  represents the absorption coefficient,  $A$  is a constant,  $h\nu$  is the photon energy ( $h$  is Planck's constant and  $\nu$  is the light frequency),  $E_g$  is the optical band gap, and the exponent  $n$  is a constant that determines the type of optical transition, i.e., for indirect allowed transitions,  $n = 2$ ; for indirect forbidden transitions,  $n = 3$ ; for direct allowed transitions,  $n = 1/2$ ; and for direct forbidden transitions,  $n = 3/2$ .  $\alpha$ -Fe<sub>2</sub>O<sub>3</sub> is known to be a direct semiconductor so  $n$  was set as  $1/2$  [28].

The magnetic properties were measured at room temperature and field with a Quantum Design Physical Properties Measurement System under an applied magnetic field sweeping from  $-50$  to  $50$  kOe.

### 2.3 Photocatalytic performance

The photocatalytic activities of the as-prepared samples were analyzed based on the photo-degradation of MB at room temperature. In a typical photocatalytic experiment,  $0.05$  g of the sample was dispersed in MB aqueous solution. Before applying the irradiation, the suspension was magnetically stirred for  $30$  min in the dark to ensure that an

adsorption–desorption equilibrium was reached between the photocatalyst powders and the aqueous dye solution. During the experiment,  $5$  mL of sample suspension was drawn from the cell at certain time intervals and the photocatalyst powder was separated with centrifugation. The residual MB concentration was analyzed with UV–Vis spectrophotometer (Shimadzu UV-2450) at  $664$  nm. The  $C/C_0$  is used to illustrate the percentage of MB degradation, where  $C$  is the MB concentration at each experimental interval, and  $C_0$  is the initial concentration after the adsorption/desorption equilibrium is reached.

## 3 Results and discussion

### 3.1 X-ray diffraction studies

X-ray diffraction technique is used to identify and determine the crystalline phase, phase structure, and crystallite size of the products. The XRD patterns of  $\alpha$ -Fe<sub>2</sub>O<sub>3</sub>@TiO<sub>2</sub> nanocomposites samples are revealed in Fig. 1. In addition, pure  $\alpha$ -Fe<sub>2</sub>O<sub>3</sub> nanoparticles and anatase TiO<sub>2</sub> nanoparticles are used for comparison. As observed in the XRD patterns of the samples, all the intensive diffraction peaks can be well indexed to rhombohedral hematite ( $\alpha$ -Fe<sub>2</sub>O<sub>3</sub>) and anatase (TiO<sub>2</sub>) marked with star (\*). After coating with anatase TiO<sub>2</sub>, several additional peaks located at  $25.34^\circ$ ,  $37.79^\circ$ ,  $48.03^\circ$ , and  $55.06^\circ$  appeared on the  $\alpha$ -Fe<sub>2</sub>O<sub>3</sub>@TiO<sub>2</sub> nanocomposite samples are indexed to the anatase phase of TiO<sub>2</sub> [12, 29], which cannot be seen on Fe<sub>2</sub>O<sub>3</sub> [30]. However, the intensity of these peaks increases regularly with the increase of TiO<sub>2</sub> content from  $10$  to  $50\%$ . This result confirms the successful conversion of TiO<sub>2</sub> into  $\alpha$ -Fe<sub>2</sub>O<sub>3</sub>@TiO<sub>2</sub>. No

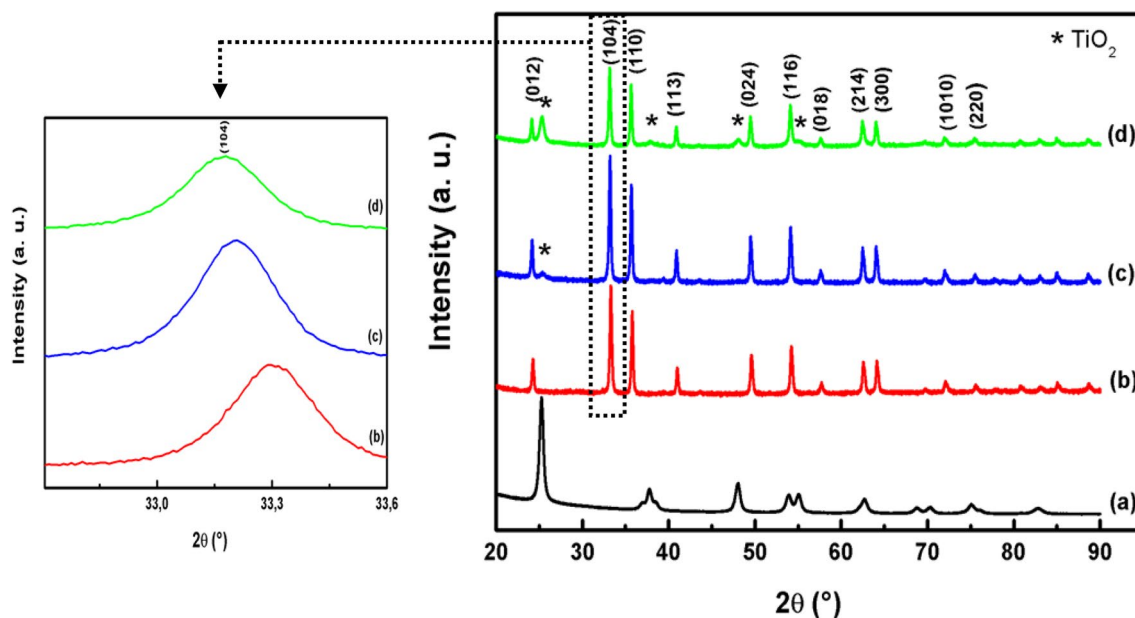


**Fig. 1** XRD patterns of **a** TiO<sub>2</sub>, **b**  $\alpha$ -Fe<sub>2</sub>O<sub>3</sub>, **c**  $\alpha$ -Fe<sub>2</sub>O<sub>3</sub>@10% TiO<sub>2</sub>, and **d**  $\alpha$ -Fe<sub>2</sub>O<sub>3</sub>@50% TiO<sub>2</sub>

other impurity peaks are detected, indicating the high phase purity of  $\alpha$ -Fe<sub>2</sub>O<sub>3</sub>@TiO<sub>2</sub> nanocomposites, which is in accord with the results reported by Xia et al. [21].

On the other hand, the enlargement of the XRD patterns of  $\alpha$ -Fe<sub>2</sub>O<sub>3</sub>,  $\alpha$ -Fe<sub>2</sub>O<sub>3</sub>@10% TiO<sub>2</sub>, and  $\alpha$ -Fe<sub>2</sub>O<sub>3</sub>@50% TiO<sub>2</sub> in the range from  $2\theta = 32.7^\circ$  to  $33.6^\circ$  show clear a shift in the angular positions of the peaks compared to pure  $\alpha$ -Fe<sub>2</sub>O<sub>3</sub> nanoparticles, suggesting that the Ti<sup>4+</sup> is successfully incorporated into the crystal lattice of hematite  $\alpha$ -Fe<sub>2</sub>O<sub>3</sub> and formed the Fe–O–Ti bond. Accordingly, after impregnating and annealing, the surface of the  $\alpha$ -Fe<sub>2</sub>O<sub>3</sub> nanoparticles is modified by TiO<sub>2</sub> nanoparticles [18, 20]. Chen et al. [31] elaborated Fe<sub>2</sub>O<sub>3</sub>–TiO<sub>2</sub> nanocomposite particles using pulsed laser gas-phase evaporation–liquid-phase collecting method, and they found that this composite showed a diameters of the primary particles which range from 20 to 50 nm, and the particles have a tendency to form chain connections.

Additionally, the average crystallite sizes of the products were calculated with the Debye–Scherrer formula, which are shown in Table 1. It is obvious that the grain sizes of the samples varied with the increase of TiO<sub>2</sub> content.

#### 4 Raman spectral analysis

To examine the structural properties of the as-prepared samples, Raman spectra were acquired and presented in Fig. 2. In the Raman spectrum of  $\alpha$ -Fe<sub>2</sub>O<sub>3</sub> (Fig. 2a), the peak located at 226 and 496 cm<sup>-1</sup> were assigned to A<sub>1g</sub> modes, and the four peaks at about 245, 293, 410, 613, and 814 cm<sup>-1</sup> were attributed to E<sub>g</sub> modes. These peaks correspond to the characteristic peaks of hematite ( $\alpha$ -Fe<sub>2</sub>O<sub>3</sub>) [32, 33]. As observed in Fig. 2b, the significant vibration peaks centered at around 144, 196, 398, 516, and 640 cm<sup>-1</sup> were attributed to E<sub>g</sub>, E<sub>g</sub>, B<sub>1g</sub>, A<sub>1g</sub> (or B<sub>1g</sub>), and E<sub>g</sub> modes of the anatase TiO<sub>2</sub> [11, 34]. After coating with anatase TiO<sub>2</sub>, the apparent vibration peak of anatase TiO<sub>2</sub> at 144 cm<sup>-1</sup> was present in  $\alpha$ -Fe<sub>2</sub>O<sub>3</sub>@10% TiO<sub>2</sub> and  $\alpha$ -Fe<sub>2</sub>O<sub>3</sub>@50% TiO<sub>2</sub>. In addition to this peak, a very weak peak at 659 cm<sup>-1</sup> [35, 36] was also detected in the two samples. Pérez et al. [37] indicate that this peak is characteristic of hematite and related to disorder.

**Table 1** Summary of physicochemical properties of TiO<sub>2</sub>,  $\alpha$ -Fe<sub>2</sub>O<sub>3</sub>,  $\alpha$ -Fe<sub>2</sub>O<sub>3</sub>@10% TiO<sub>2</sub>, and  $\alpha$ -Fe<sub>2</sub>O<sub>3</sub>@50% TiO<sub>2</sub>

Samples	Peak position $2\theta$ (°)	Average crystallite size (nm)	Band gap (eV)	Magnetic parameters	
				Hc (Oe)	Mr (emu/g)
TiO <sub>2</sub>	(101) 25.34	12.45	3.19	–	–
$\alpha$ -Fe <sub>2</sub> O <sub>3</sub>	(104) 33.24	36.86	2.07	2600.0	0.107
$\alpha$ -Fe <sub>2</sub> O <sub>3</sub> @ 10% TiO <sub>2</sub>	(104) 33.20	38.07	2.09	2138.6	0.099
$\alpha$ -Fe <sub>2</sub> O <sub>3</sub> @ 50% TiO <sub>2</sub>	(104) 33.16	37.66	2.13	2290.3	0.066

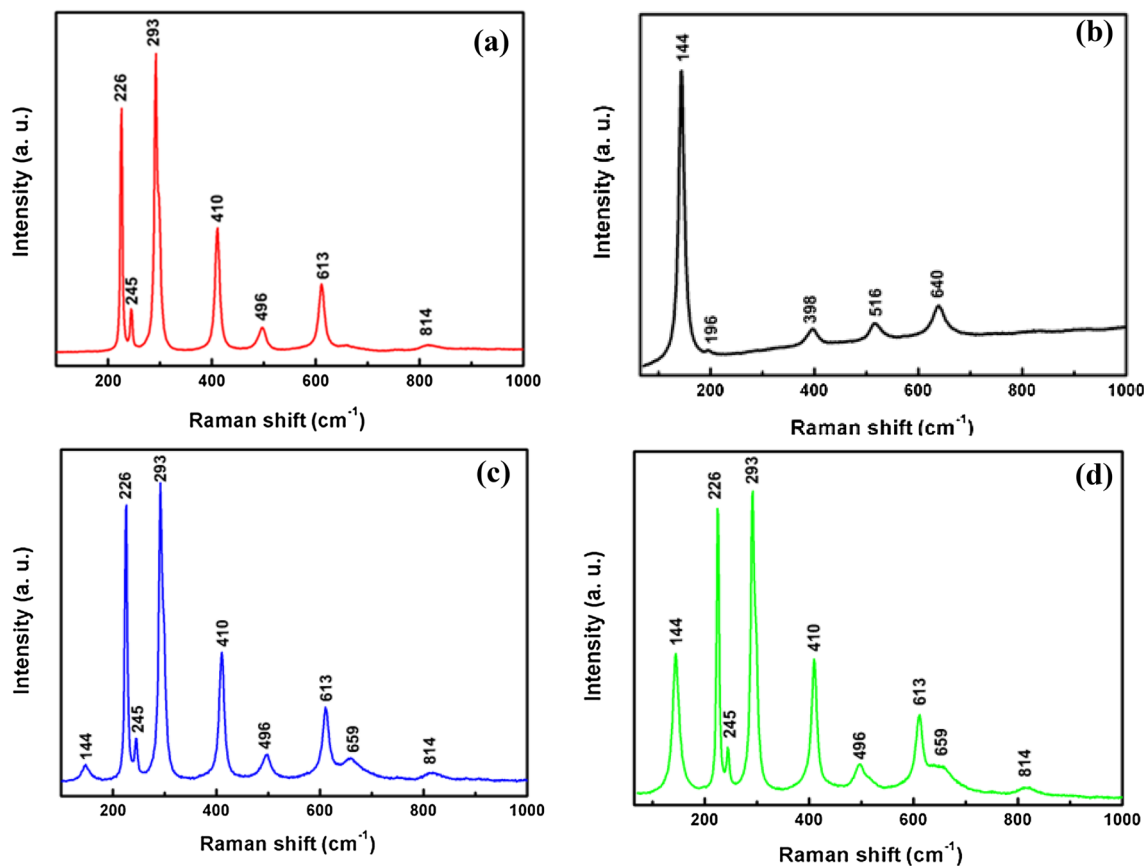


**Fig. 2** Raman spectra of **a**  $\alpha$ -Fe<sub>2</sub>O<sub>3</sub>, **b** TiO<sub>2</sub>, **c**  $\alpha$ -Fe<sub>2</sub>O<sub>3</sub>@10% TiO<sub>2</sub>, and **d**  $\alpha$ -Fe<sub>2</sub>O<sub>3</sub>@50% TiO<sub>2</sub>

#### 4.1 TEM observations

To get more information about the structure, the composite samples were characterized by TEM. Figure 3 shows the typical TEM image of  $\alpha$ -Fe<sub>2</sub>O<sub>3</sub>, TiO<sub>2</sub>,  $\alpha$ -Fe<sub>2</sub>O<sub>3</sub>@10% TiO<sub>2</sub>, and  $\alpha$ -Fe<sub>2</sub>O<sub>3</sub>@50% TiO<sub>2</sub>. It can be clearly seen that all the samples exhibit spherical morphology. The particle size of  $\alpha$ -Fe<sub>2</sub>O<sub>3</sub> (Fig. 3a) ranged between 35 and 40 nm. Furthermore, the TEM images of pure TiO<sub>2</sub> (Fig. 3b) indicated that the grain size was homogenous and fairly small (about 15 nm). This value is close to the crystallite size estimated by XRD, as shown in Table 1. Moreover, the core-shell structure was clearly observed from the TEM micrograph (Fig. 3c, d). It can be found that the diameter of the core was about 40 nm and the shell thickness was about 5 nm. These results are in good accordance with those found by Chen et al. [24]. Based on the TEM images, the  $\alpha$ -Fe<sub>2</sub>O<sub>3</sub>@TiO<sub>2</sub> nanocomposites samples were prepared successfully using a simple co-precipitation technique. These results were in agreement with that of XRD.

#### 4.2 SEM observations

The surface morphological study of the  $\alpha$ -Fe<sub>2</sub>O<sub>3</sub>@TiO<sub>2</sub> nanocomposites was carried out using SEM. It can be seen in Fig. 4 that the TiO<sub>2</sub> nanoparticles are deposited on surface of  $\alpha$ -Fe<sub>2</sub>O<sub>3</sub> nanoparticles. Which suggest that the  $\alpha$ -Fe<sub>2</sub>O<sub>3</sub>@TiO<sub>2</sub> nanocomposites are successful prepared. Also, the SEM image shows that dimensional distribution is not uniform: Fig. 4a indicates that the grain size of pure TiO<sub>2</sub> was homogenous and fairly small. However, Fig. 4b shows that  $\alpha$ -Fe<sub>2</sub>O<sub>3</sub> nanoparticles are agglomerated and randomly distributed. Figure 4c, d shows that the shape of the  $\alpha$ -Fe<sub>2</sub>O<sub>3</sub>@TiO<sub>2</sub> differs slightly by changing the concentration of TiO<sub>2</sub>. These results were in agreement with that of XRD and TEM.

#### 4.3 Optical analysis

To investigate the UV-Vis absorbance of  $\alpha$ -Fe<sub>2</sub>O<sub>3</sub>@TiO<sub>2</sub> nanocomposites, the diffuse-reflectance spectra are obtained. The UV-Vis DRS of pure TiO<sub>2</sub> and  $\alpha$ -Fe<sub>2</sub>O<sub>3</sub> nanoparticles

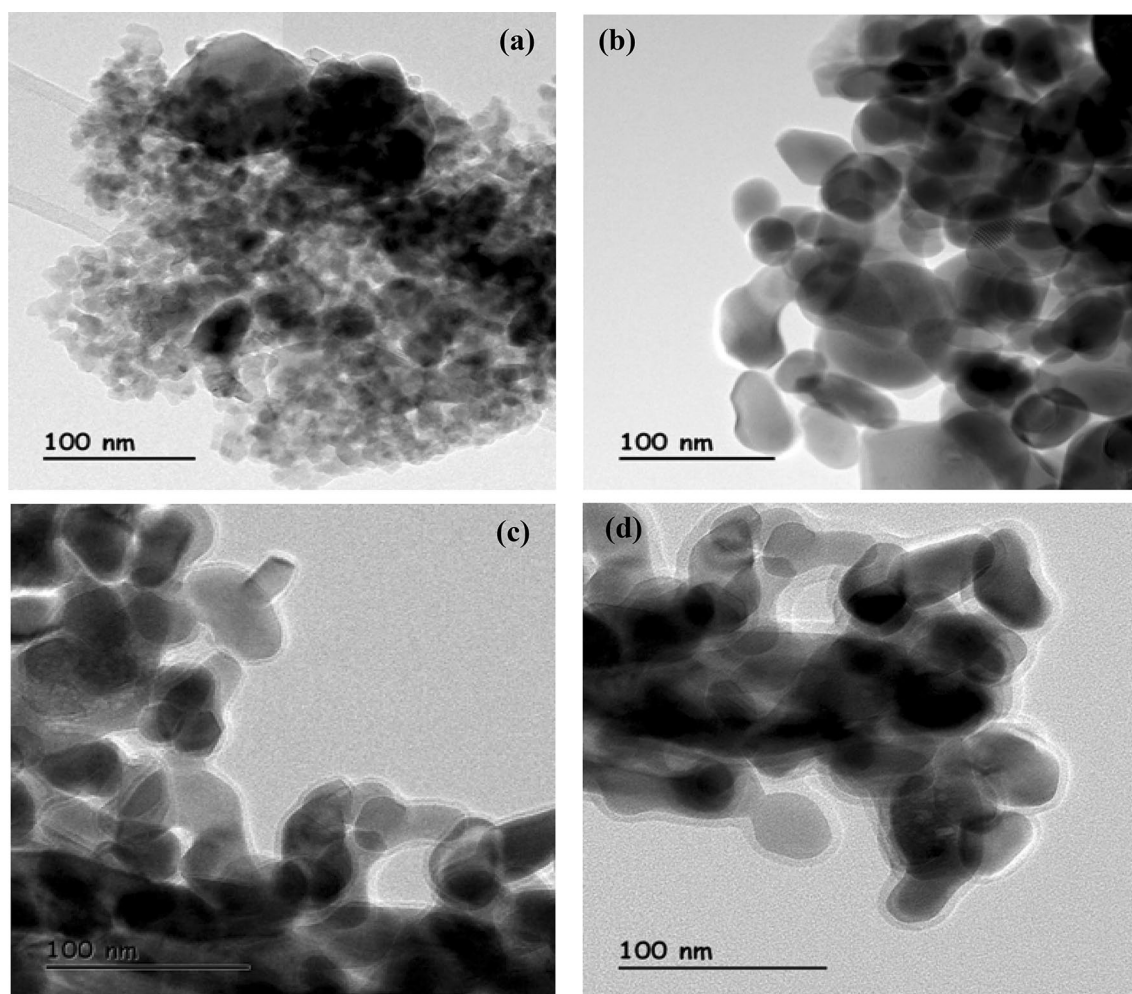


**Fig. 3** TEM micrograph of **a**  $\alpha$ -Fe<sub>2</sub>O<sub>3</sub>, **b** TiO<sub>2</sub>, **c**  $\alpha$ -Fe<sub>2</sub>O<sub>3</sub>@10% TiO<sub>2</sub>, and **d**  $\alpha$ -Fe<sub>2</sub>O<sub>3</sub>@50% TiO<sub>2</sub>

are also evaluated for comparison. As demonstrated in Fig. 5, the absorption edges of pure TiO<sub>2</sub> are around 400 nm [12, 29]. For pure  $\alpha$ -Fe<sub>2</sub>O<sub>3</sub> nanoparticles, obvious visible absorption is observed in the curve ( $\lambda \approx 600$  nm) [38]. In the contrast, the  $\alpha$ -Fe<sub>2</sub>O<sub>3</sub>@TiO<sub>2</sub> nanocomposites exhibited not only stronger absorption in the ultra-violet region of less than 400 nm but also adequate and strong absorption in the visible-light region of 400–700 nm [8, 39]. This will undoubtedly improve the photocatalytic activity of the nanocomposites photocatalyst.

Figure 6 show the plots of  $(ah\nu)^2$  versus energy ( $h\nu$ ) for the band-gap energies of TiO<sub>2</sub>,  $\alpha$ -Fe<sub>2</sub>O<sub>3</sub>,  $\alpha$ -Fe<sub>2</sub>O<sub>3</sub>@10% TiO<sub>2</sub>, and  $\alpha$ -Fe<sub>2</sub>O<sub>3</sub>@50% TiO<sub>2</sub>, which were calculated based on the optical absorption edge obtained from UV–Vis DRS spectra using Eq. (2). The results show that the band-gap energies of  $\alpha$ -Fe<sub>2</sub>O<sub>3</sub>@10% TiO<sub>2</sub> and  $\alpha$ -Fe<sub>2</sub>O<sub>3</sub>@50% TiO<sub>2</sub> are approximately 2.09 and 2.13 eV, respectively (Table 1). In the present condition, Fe<sup>3+</sup> was doped with the TiO<sub>2</sub> lattice, resulted in the increasing of the band gap. Additionally,

the band gap of  $\alpha$ -Fe<sub>2</sub>O<sub>3</sub> was only 2.07 eV. The presence of this band-gap semiconductor, as well as the TiO<sub>2</sub> band gap [40], greatly ameliorated the light absorption properties of the  $\alpha$ -Fe<sub>2</sub>O<sub>3</sub>@TiO<sub>2</sub> nanocomposites, and enabled the absorption of visible light [6, 14]. According to the results of UV–Vis DRS, the as-prepared  $\alpha$ -Fe<sub>2</sub>O<sub>3</sub>@TiO<sub>2</sub> nanocomposites are expected to exhibit excellent photocatalytic activity for degrading organic contaminants in the visible region, which corresponded to the photo-degradation process.

#### 4.4 Magnetic analysis

Vibrating sample magnetometer (VSM) was employed to study the magnetic properties of prepared  $\alpha$ -Fe<sub>2</sub>O<sub>3</sub>@TiO<sub>2</sub> nanocomposites. The measurement was performed at room temperature, with the field sweeping from – 50 to 50 kOe. As shown in Fig. 7, the magnetization measurement result of all the samples is indicative of the presence of ferromagnetic components [28, 40]. In addition, it can be seen that no

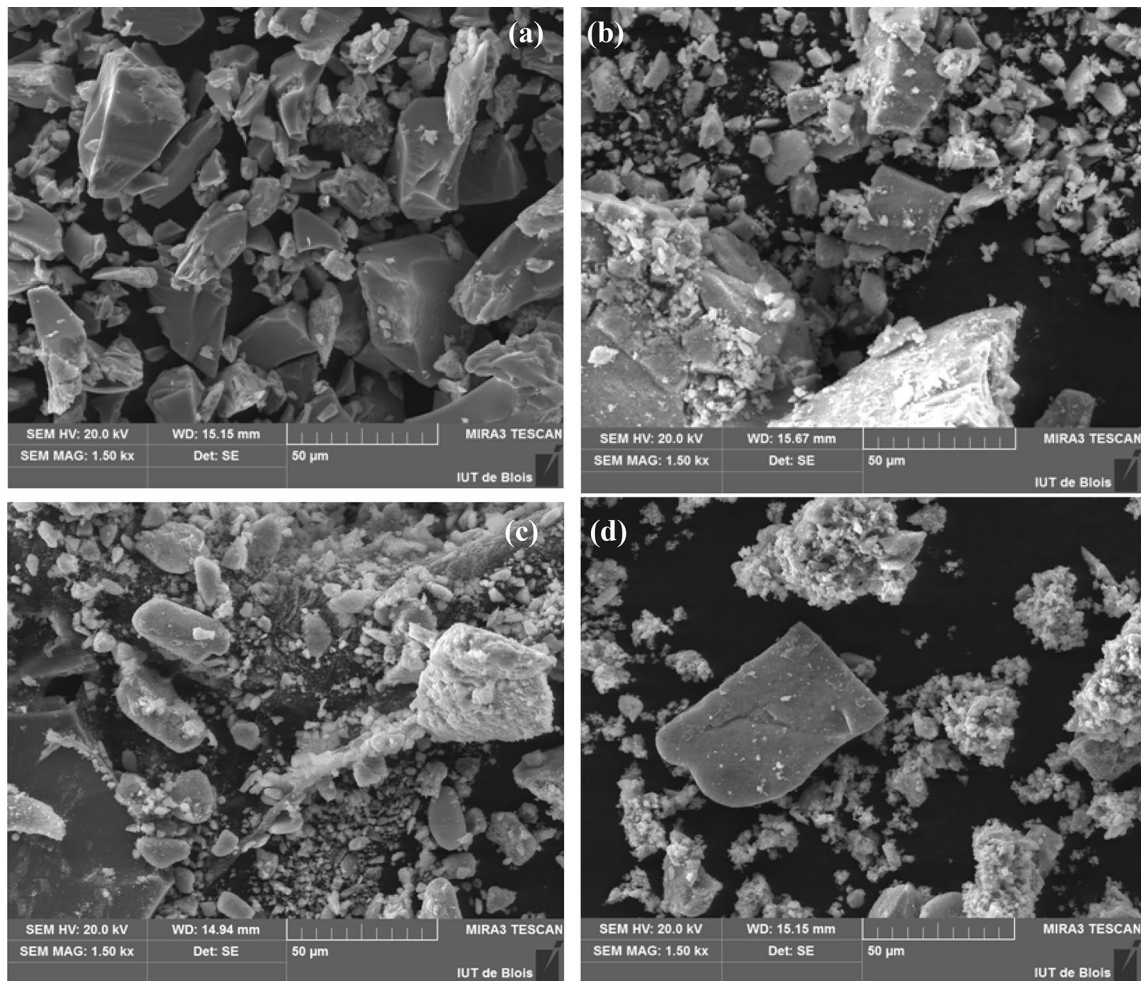


Fig. 4 SEM image of the TiO<sub>2</sub>,  $\alpha$ -Fe<sub>2</sub>O<sub>3</sub> and  $\alpha$ -Fe<sub>2</sub>O<sub>3</sub>@TiO<sub>2</sub> nanocomposites samples

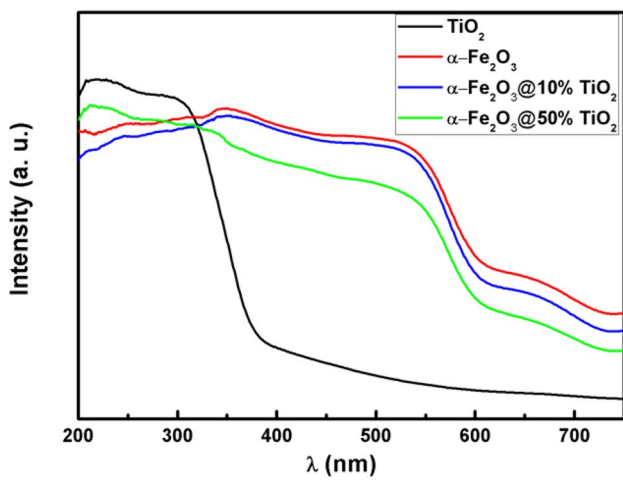


Fig. 5 Absorption spectra of TiO<sub>2</sub>,  $\alpha$ -Fe<sub>2</sub>O<sub>3</sub>,  $\alpha$ -Fe<sub>2</sub>O<sub>3</sub>@10% TiO<sub>2</sub> and  $\alpha$ -Fe<sub>2</sub>O<sub>3</sub>@50% TiO<sub>2</sub>

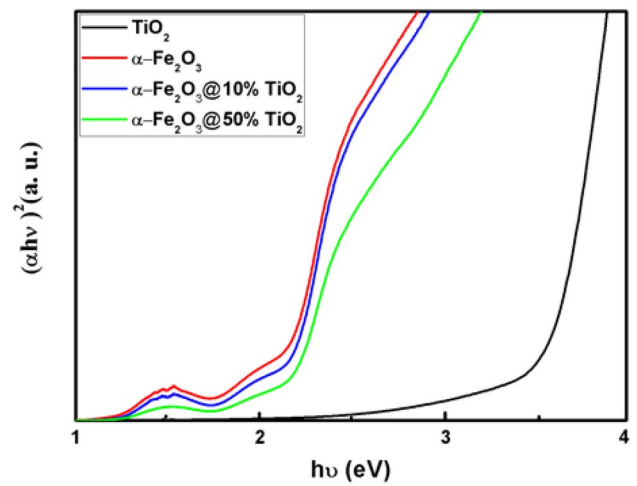
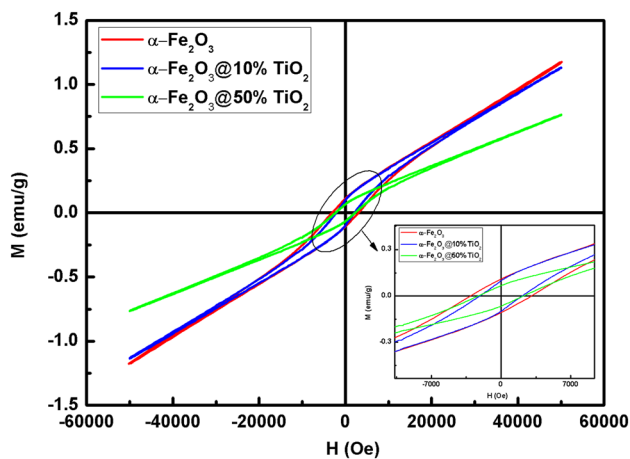


Fig. 6 Plots of  $(\alpha h\nu)^2$  versus  $h\nu$  of TiO<sub>2</sub>,  $\alpha$ -Fe<sub>2</sub>O<sub>3</sub>,  $\alpha$ -Fe<sub>2</sub>O<sub>3</sub>@10% TiO<sub>2</sub> and  $\alpha$ -Fe<sub>2</sub>O<sub>3</sub>@50% TiO<sub>2</sub>



**Fig. 7** Hysteresis loops of  $\alpha$ -Fe<sub>2</sub>O<sub>3</sub>,  $\alpha$ -Fe<sub>2</sub>O<sub>3</sub>@10% TiO<sub>2</sub> and  $\alpha$ -Fe<sub>2</sub>O<sub>3</sub>@50% TiO<sub>2</sub>

saturation of the magnetization as a function of the field is observed up to the maximum applied magnetic field. These results are in a good agreement with those obtained in the literature [16, 24].

The magnetic parameters consisting of H<sub>c</sub> and M<sub>r</sub> of the synthesized  $\alpha$ -Fe<sub>2</sub>O<sub>3</sub>,  $\alpha$ -Fe<sub>2</sub>O<sub>3</sub>@10% TiO<sub>2</sub>, and  $\alpha$ -Fe<sub>2</sub>O<sub>3</sub>@50% TiO<sub>2</sub> are summarized in Table 1, where H<sub>c</sub> is the coercive force and M<sub>r</sub> is the remnant magnetization. As seen from Table 1, the H<sub>c</sub> and M<sub>r</sub> values of the  $\alpha$ -Fe<sub>2</sub>O<sub>3</sub> are higher than the other samples. The reduction in the magnetic parameters might be because the TiO<sub>2</sub> shell does not contribute to the magnetization, which then leads to the smaller magnetic moment per unit mass.

#### 4.5 Photocatalytic activity

To investigate the photocatalytic degradation of organic pollutants with the nanoparticles under visible light, MB was selected as a model contaminant for photocatalytic decolorization [41, 42]. The photocatalytic performance during the degradation of MB using different catalysts under irradiation with visible light is illustrated in Fig. 8. Under the visible-light irradiation, TiO<sub>2</sub> cannot be excited to generate electron–hole pairs, show poor photocatalytic activity on MB degradation, probably because it contains anatase which has a band gap of 3.1 eV resulting in ultra-violet absorption [12]. While  $\alpha$ -Fe<sub>2</sub>O<sub>3</sub> displays strong response to visible-light irradiation, it exhibits slight photocatalytic degradation on MB. It is due to the fact that the photo-induced electron–hole pairs in pure  $\alpha$ -Fe<sub>2</sub>O<sub>3</sub> are difficult to separate and strongly intend to recombine, thus inducing poor photocatalytic activity [43, 44].

Zhan et al. [45] elaborated the mesoporous Fe<sub>2</sub>O<sub>3</sub>-doped TiO<sub>2</sub> nanostructured fibers, and they found that this composite showed that the photocatalytic activity was

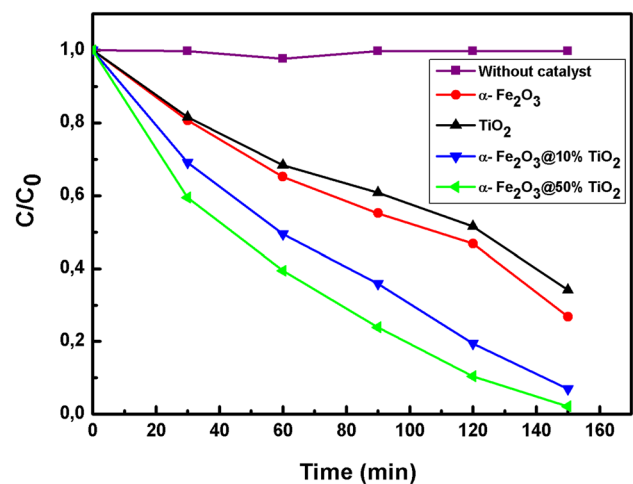


**Fig. 8** Photo-degradation of MB in the presence of different catalysts under visible light irradiation

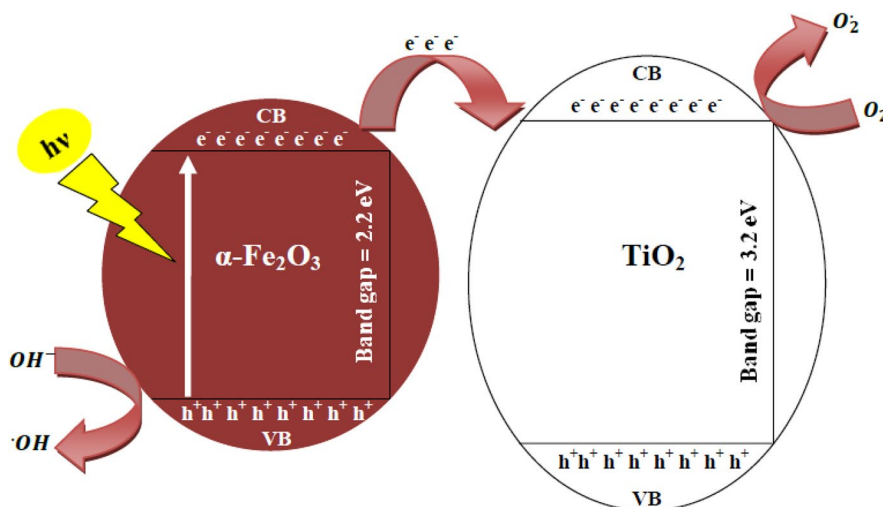
evaluated by photocatalytic degradation of MB in water under UV irradiation. Compared with different types of photocatalysts, the 1% Fe<sub>2</sub>O<sub>3</sub>-doped TiO<sub>2</sub> fibers exhibited super photocatalytic activity.

After 120 min of visible-light irradiation, about 92% of MB degradation was observed with the use of  $\alpha$ -Fe<sub>2</sub>O<sub>3</sub>@50% TiO<sub>2</sub> nanocomposites, whereas much lower than the decoloration rate of 51.1% over pure  $\alpha$ -Fe<sub>2</sub>O<sub>3</sub> nanoparticles was achieved. After 150 min of visible-light irradiation, the major absorbance peaks of MB degraded by  $\alpha$ -Fe<sub>2</sub>O<sub>3</sub>@50% TiO<sub>2</sub> nanocomposites completely disappeared, whereas there was still 26.5% of MB left when degraded by pure  $\alpha$ -Fe<sub>2</sub>O<sub>3</sub> nanoparticles. These results were better than that observed one with other model pollutant reported by Zhang et al. [8]. Therefore, the TiO<sub>2</sub> content should be an important factor affecting the photocatalytic activity of the  $\alpha$ -Fe<sub>2</sub>O<sub>3</sub>@TiO<sub>2</sub> nanocomposite. It is obvious that the coupled  $\alpha$ -Fe<sub>2</sub>O<sub>3</sub>/TiO<sub>2</sub> photocatalyst displayed higher photocatalytic activity than pure  $\alpha$ -Fe<sub>2</sub>O<sub>3</sub> and TiO<sub>2</sub>, and the photocatalytic activity changed with the different molar ratio of Fe to Ti. These results are in good accordance with those found by Tang et al. [16].

From these results,  $\alpha$ -Fe<sub>2</sub>O<sub>3</sub>@TiO<sub>2</sub> nanocomposites show the better photocatalytic performance than the corresponding  $\alpha$ -Fe<sub>2</sub>O<sub>3</sub> and TiO<sub>2</sub> monocomponent photocatalysts, because the nanostructures with a magnetic core, covered by TiO<sub>2</sub> nanoparticles (shell), aggregate the TiO<sub>2</sub> adsorption features, due to chemical affinity, and the magnetic properties of the iron oxide. The combination of both properties in a nanoscale structure allows predicting applications of magnetite nanoparticles in effluent treatment systems. This method provides a quick and efficient separation of the nanoparticles dispersed in MB



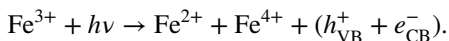
**Scheme 2** Schematic illustration of photocatalytic mechanism using  $\alpha\text{-Fe}_2\text{O}_3@/\text{TiO}_2$  nanocomposites under visible light



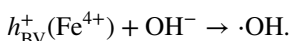
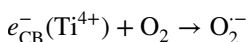
aqueous solution, since after adsorption, the samples can be removed in a continuous process by the use of magnetic fields outside of pipelines, which are projected to attend this function.

#### 4.6 Possible photocatalytic mechanism

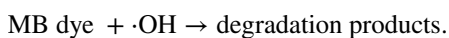
The possible process of the photocatalytic mechanism of  $\alpha\text{-Fe}_2\text{O}_3@/\text{TiO}_2$  nanocomposites has been proposed and is shown in Scheme 2. Under the visible-light irradiation,  $\text{TiO}_2$  cannot be excited to generate electron–hole pairs, whereas  $\alpha\text{-Fe}_2\text{O}_3$  could be easily activated and yields photogenerated electrons from the valence band (VB) to its conduction band (CB). Subsequently, the excited electrons of  $\alpha\text{-Fe}_2\text{O}_3$  can immigrate to the conduction band (CB) of  $\text{TiO}_2$  by the action of built-in electric field and the concentration gradient, while photogenerated holes accumulated in the valence band of  $\alpha\text{-Fe}_2\text{O}_3$ :



The electrons in the conduction band (CB) of  $\text{TiO}_2$  will react with molecular oxygen  $\text{O}_2$  dissolved in the MB solution to form the superoxide anion  $\text{O}_2^-$ . While the accumulated holes in the valence band (VB) of  $\alpha\text{-Fe}_2\text{O}_3$  will react with  $\text{OH}^-$  to produce reactive hydroxyl radicals ( $\cdot\text{OH}$ ):



The resultant  $\cdot\text{OH}$  will further decompose the organic substance effectively as a powerful oxidant.



## 5 Conclusion

In summary,  $\alpha\text{-Fe}_2\text{O}_3@/\text{TiO}_2$  nanocomposites were synthesized by co-precipitation method and their photocatalytic activities were investigated too. The detailed morphological and structural characterizations revealed that the obtained structure is mainly composed of anatase  $\text{TiO}_2$  phase and  $\alpha\text{-Fe}_2\text{O}_3$  phase. Catalytic experiments showed that all prepared samples are photocatalytically active. While  $\alpha\text{-Fe}_2\text{O}_3@50\%$   $\text{TiO}_2$  sample exhibited the highest photocatalytic activity among other prepared materials due to its superior properties. Enhanced light absorption and magnetic properties play important roles to enhanced photocatalytic activity. The produced nanomaterials showed enhanced photocatalytic performance in the visible region for the degradation of organic dye and excellent cycling properties as compared to their corresponding nanomaterials prepared with chemical method.

## References

1. D.R. Zhang, H.L. Liu, S.Y. Han, W.X. Piao, J. Ind. Eng. Chem. **19**, 1838–1844 (2013)
2. J.Q. Li, D.F. Wang, Z.Y. Guo, Z.F. Zhu, Appl. Surf. Sci. **263**, 382–388 (2012)
3. F.A. Harraz, A.A. Ismail, S.A. Al-Sayari, A. Al-Hajry, J. Photochem. Photobiol. A. **299**, 18–24 (2015)
4. A. Umar, M.S. Akhtar, G.N. Dar, S. Baskoutas, Talanta **116**, 1060–1066 (2013)
5. G.K. Mor, H.E. Prakasam, O.K. Varghese, K. Shankar, C.A. Grimes, Letters. **7**, 2356–2364 (2007)
6. W. Wu, X. Xiao, S. Zhang, F. Ren, C. Jiang, Nanoscale Res. Lett. **6**, 533 (2011)
7. M. Mishra, D.M. Chun, Appl. Catal. A General **498**, 126–141 (2015)
8. X. Zhang, Y. Xie, H. Chen, J. Guo, A. Meng, C. Li, Appl. Surf. Sci. **317**, 43–48 (2014)

9. J. Liu, S. Yang, W. Wu, Q. Tian, S. Cui, Z. Dai, F. Ren, X. Xiao, C. Jiang, *Chem. Eng.* **3**, 2975–2984 (2015)
10. D. Liú, Z. Li, W. Wang, G. Wang, D. Liú, *J. Alloys Compd.* **654**, 491–497 (2016)
11. S.K. Tripathy, T. Sahoo, M. Mohapatra, S. Anand, Y.T. Yu, J. Phys. Chem. Solids. **70**, 147–152 (2009)
12. H. Mansour, R. Bargougui, A. Gadri, S. Ammar, *J Mater Sci Mater Electron* **2**, 0854–5736 (2016)
13. N. Abbas, G.N. Shao, M.S. Haider, S.M. Imran, S.S. Park, H.T. Kim, *J. Ind. Eng. Chem.* **39**, 112–120 (2016)
14. S. Liu, J. Zhu, X. Guo, J. Ge, H. Wu, *Colloids Surf. A Physico. Chem. Eng. Aspects* **484**, 434–440 (2015)
15. H. Zhao, W. Fu, H. Yang, Y. Xu, W. Zhao, Y. Zhang, H. Chen, Q. Jing, X. Qi, J. Cao, X. Zhou, Y. Li, *Appl. Surf. Sci.* **257**, 8778–8783 (2011)
16. H. Tang, D. Zhang, G. Tang, X. Ji, W. Lia, C. Lia, X. Yang, *Ceram. Int.* **39**, 8633–8640 (2013)
17. J. Zhu, S. Liu, J. Ge, X. Guo, X. Wang, H. Wu, *Res Chem Intermed* **6**, 1164–2236 (2015)
18. K. Yao, P. Basnet, H. Sessions, G.K. Larsen, S.E.H. Murph, Y. Zhao, *Catal. Today.* **270**, 51–58 (2016)
19. B.A. Feiz, S. Aber, A. Khataee, E. Alipour, *J. Mol. Catal. A: Chem.* **395**, 440–448 (2014)
20. Y. Fu, Q. Wei, X. Wang, H. Shu, X. Yang, S. Sun, *Mater. Chem. A* **3**, 13807 (2015)
21. Y. Xia, L. Yin, *Phys. Chem. Chem. Phys.* **15**, 18627 (2013)
22. D. Wodka, R.P. Socha, E. Bielańska, M. Elżbiaciak-Wodka, P. Nowak, P. Warszyński, *Appl. Surf. Sci.* **319**, 173 (2014)
23. A. Banisharif, A. Ali Khodadadi, Y. Mortazavi, A.A. Firooz, J. Beheshtian, S. Agah, S. Menbari, *Appl. Catal. B Environ.* **165**, 209 (2015)
24. S. Chen, Y. Zhang, W. Han, D. Wellburn, J. Liang, C. Liu, *Appl. Surf. Sci.* **283**, 422–429 (2013)
25. J.Q. Li, Z.X. Liu, D.F. Wang, Z.F. Zhu, *Mater. Sci. Semicond. Process.* **27**, 950–957 (2014)
26. B.D. Cullity, *Elements of X-Ray Diffraction* (Addison-Wesley, Boston, 1978), p. 102
27. M. Khan, J. Xu, N. Chen, W. Cao, *J. Alloys Comp.* **513**, 539 (2012)
28. K. Raja, M.M. Jaculine, M. Jose, S. Verma, A.A.M. Prince, K. Ilangovan, K. Sethusankar, S.J. Das, *Superlattices Microstruct.* **86**, 306–312 (2015)
29. H. Slimen, A. Houas, J.P. Nogier, *J. Photochem. Photobiol. A.* **221**, 13–21 (2011)
30. X. Zheng, Y. Jia, F. Chai, F. Qu, A. Umar, X. Wu, *J. Colloid Interface Sci.* **457**, 345–352 (2015)
31. S. Chen, Y. Zhang, W. Han, D. Wellburn, J. Liang, C. Liu, *Appl. Surf. Sci.* **283**, 422–429 (2013)
32. Y.S. Cho, Y.D. Huh, *Bull. Korean Chem. Soc.* **30**, 1413 (2009)
33. Q. Wei, Z. Zhang, Z. Li, Q. Zhou, Y. Zhu, *J. Phys. D Appl. Phys.* **41**, 202002 (2008)
34. B. Liu, X. Wang, G. Cai, L. Wen, Y. Song, X. Zhao, *J. Hazard. Mater.* **169**, 1112–1118 (2009)
35. D. Bersani, P.P. Lottici, A. Montenero, *J. Raman Spectrosc.* **30**, 355 (1999)
36. D.L.A. de Faria, F.N. Lopes, *Vib. Spectrosc.* **45**, 117–121 (2007)
37. C. Pérez León, L. Kado, M. Zhang, A.H.E. Müller, *J. Raman Spectrosc.* **35**, 165 (2004)
38. M.A. Valenzuela, P. Bosch, J.J. Becerrill, O. Quiroz, A.I. Páez, *J. Photochem. Photobiol. A.* **148**, 177–182 (2002)
39. A. Bazmara, S. Mohammadnejad, *Optik* **125**, 5733–5737 (2014)
40. Z.N. Kayania, A. Afzal, M.Z. Butt, I. Batool, S. Arshad, Y. Alia, S. Riaz, S. Naseem, *Mater. Today Proc.* **2**, 5660–5663 (2015)
41. W. Smith, Y.P. Zhao, *Catal. Commun.* **10**, 1117–1121 (2009)
42. M. Mrowetz, W. Balcerski, A.J. Colussi, M.R. Hoffmann, *J. Phys. Chem. B.* **108**, 17269–17273 (2004)
43. H. Zhang, B. Han, J. Meng, *J. Nanosci. Nanotechnol.* **16**, 12433–12443 (2016)
44. A. Amarjargal, Z. Jiang, L.D. Tijing, C. Hee Park, I.T. Im, C.S. Kim, *J. Alloys Comp.* **580**, 143–147 (2013)
45. S. Zhan, Yu. Jiangyao Yang, N.W. Liu, J. Dai, Yu. Hongbing, X. Gao, Yi Li, *J Colloid Interface Sci* **355**, 328–333 (2011)

**Publisher's Note** Springer Nature remains neutral with regard to jurisdictional claims in published maps and institutional affiliations.